Modeling impedance boundary conditions and acoustic barriers using the Immersed Boundary Method

Citation for published version:
Bilbao, S 2023, 'Modeling impedance boundary conditions and acoustic barriers using the Immersed Boundary Method: The three-dimensional case', *The Journal of the Acoustical Society of America*, vol. 154, no. 2, pp. 874-885. https://doi.org/10.1121/10.0020635

Digital Object Identifier (DOI):
10.1121/10.0020635

Link:
Link to publication record in Edinburgh Research Explorer

Document Version:
Publisher's PDF, also known as Version of record

Published In:
The Journal of the Acoustical Society of America

AUGUST 11 2023

Modeling impedance boundary conditions and acoustic barriers using the immersed boundary method: The three-dimensional case

Stefan Bilbao

J Acoust Soc Am 154, 874–885 (2023)
https://doi.org/10.1121/10.0020635

JASA ARTICLE

Modeling impedance boundary conditions and acoustic barriers using the immersed boundary method: The three-dimensional case[a]

Stefan Bilbao[b]
Acoustics and Audio Group, University of Edinburgh, Room 2.10 Alison House, 12 Nicolson Square, Edinburgh EH8 9DF, United Kingdom

ABSTRACT:
One of the main challenges in time domain wave-based acoustics is the accurate simulation of both boundary conditions and barriers capable of reflecting and transmitting energy. Such scattering structures are generally of irregular geometry and characterised in terms of frequency-dependent reflectances and transittances. Conditions for numerical stability can be difficult to obtain in either case. Immersed boundary methods, which are heavily used in computational fluid dynamics applications, replace boundaries by discrete driving terms, avoiding volumetric meshing and staircasing approaches altogether. The main contribution of this article is a unified numerical treatment of both impedance boundary conditions and barriers capable of transmitting energy and suitable for use in the setting of wave-based acoustics. It is framed in terms of the immersed boundary method within a finite difference time domain scheme, using a dual set of matched discrete driving terms in both the conservation of mass and momentum equations that can be tuned against a desired reflectance or transmittance. Numerical results in three dimensions are presented, illustrating non-porous barriers and impedance boundary conditions, and highlight important features such as spurious leakage through an immersed boundary. A brief demonstration of conditions for numerical stability of the immersed boundary method in this context is provided in an appendix. https://doi.org/10.1121/10.0020635

(Received 16 March 2023; revised 19 July 2023; accepted 27 July 2023; published online 11 August 2023)

[Editor: Lauri Savioja] Pages: 874–885

I. INTRODUCTION

Volumetric wave-based time domain simulation for applications in room and architectural acoustics has a long history. Many frameworks have emerged, including finite difference time domain (FDTD) methods,[1–3] finite volume time domain (FVTD) methods,[4] pseudospectral time domain (PSTD) methods,[5] and methods of the finite element family, including spectral elements[6] and discontinuous Galerkin methods.[7] For such methods, there is a full volumetric meshing of the space, and the solution is computed recursively using a time-stepping procedure.

One of the main challenges is the accurate representation of bounding geometries and the accompanying conditions, usually frequency-dependent. There are two main categories: (1) boundary conditions, which do not permit transmission of energy through a surface and are usually characterised by an impedance (examples are outer wall conditions and also interior boundaries of scattering objects, such as the human head, or thin two-sided barriers that do not allow transmission) and (2) an interior two-sided barrier allowing transmission, characterised in terms of reflection and transmission coefficients. Not covered here are boundaries or barriers with in-plane dynamics. These include non-locally reactive boundary conditions[8] as well as scattering from objects such as Kirchhoff plates.[9]

One approach used in both cases above, when FVTD or methods of the finite element family are employed, is form-fitting volumetric meshing. FVTD has been used in this way[4] for impedance boundary conditions of type 1, and discontinuous Galerkin methods have recently been used to model transmission through a barrier of type 2 above.[10] However, unless the boundary aligns neatly with a structured meshing, such as a Cartesian grid, the meshing procedure can become an involved and computationally intensive preprocessing stage, possibly extending into the interior of the domain, as illustrated in a recent paper.[10] While suitable for small geometries, or in two dimensions (2D), this approach becomes infeasible for large volumes in three dimensions (3D) at near audio rates, where mesh sizes become very small (approximately 1 cm). Another more basic technique is to make use of jagged "staircased" approximations to a given boundary surface. This extremely efficient approach is often used within FDTD methods, but it has been shown to produce poor results, both in terms of the coherence of reflected responses and due to the overestimation of boundary surfaces.[4] It has also been used in the

---

[a] Preliminary results of this work were presented in "Impedance boundaries and transmission in wave-based acoustics using the immersed boundary method," International Congress on Acoustics, Gyeongju, South Korea, October 2022.

[b] Electronic mail: sbilbao@ed.ac.uk

simulation of scattering from the human head using FDTD, although the grid spacing and time step must be chosen to be very small to achieve good results.[11] Staircasing methods have also been proposed for barriers of type 2 in FDTD and demonstrated in the case of a barrier aligned with a Cartesian grid.[12] (Cut-cell techniques,[13,14] not employed in acoustics to the knowledge of this author, form a middle ground between volumetric meshing and staircasing.) Conditions for numerical stability under such terminating conditions can be demonstrated in some cases, such as FVTD, or staircased FDTD as a special case of FVTD,[4,15] but are not often investigated in detail.

In immersed boundary methods,[16–18] the boundary is replaced by a finite collection of field-dependent driving terms, and, thus, volumetric meshing and staircasing are avoided entirely, and operation is over a regular grid. Such methods have been employed extensively in nonlinear fluid dynamics problems[19,20] as well as in linear acoustics.[21] In most applications, the driving terms appear in the equation describing conservation of momentum and have the interpretation of forces. This is natural in the context of incompressible flow[19,20,22–24]—the main setting in which immersed boundaries are employed (with some exceptions[18,25]). In acoustics, however, even under linearized conditions—the starting point in virtual acoustics—flow is compressible. There is, thus, the opportunity to introduce additional driving terms in the equation describing conservation of mass and with the interpretation of a mass source. It has been shown in the one-dimensional (1D) case[26] that it is possible to use this pair of driving terms together to emulate general acoustic barriers, including the special case of a non-transmitting impedance boundary condition, within a single unified framework. When extended to 3D, this generalizes considerably the approach presented recently[27] in the context of wave-based virtual acoustics. In this linearized case, a full stability analysis is possible—provided the approach to the time domain discretisation of frequency domain boundary and barrier conditions is passivity-preserving, the immersed boundary has no impact on the stability of the resulting method.

This article is a continuation of a more fundamental study of the immersed boundary in 1D acoustics.[26] Acoustic wave propagation in three dimensions is introduced in Sec. II, alongside a formulation of the immersed boundary method, defined over arbitrary surfaces, including dual driving distributions in the mass and momentum conservation equations. These distributions are related to acoustic field variables through a pair of arbitrary passive (positive real) immittance distributions. The resulting system is then reduced to a finite number of driving terms in preparation for discretisation. FDTD methods are introduced in Sec. III, including discrete representations of the Dirac delta function and a specialised numerical integration rule for the simulation of the immittances. Although the resulting scheme is formally implicit, fast linear system solution techniques that exploit matrix structure are available. Numerical results are presented in Sec. IV, in the case of rectangular acoustic barriers and panels and scattering from a sphere under a variety of boundary conditions. Some concluding remarks appear in Sec. V. A brief stability analysis of the immersed boundary in discrete time appears in the Appendix. Preliminary results have appeared at the International Congress on Acoustics in 2022.[28]

II. IMMERSED BOUNDARIES IN THREE-DIMENSIONAL ACOUSTICS

In free space, the equations of linear acoustics in three dimensions may be written as

$$\frac{1}{\rho c^2}\partial_t p + \nabla\cdot\mathbf{v} = 0, \quad \rho\partial_t\mathbf{v} + \nabla p = \mathbf{0}. \tag{1}$$

Here, $p(\mathbf{x},t)$ and $\mathbf{v}(\mathbf{x},t) = [v_1(\mathbf{x},t), v_2(\mathbf{x},t), v_3(\mathbf{x},t)]$ are the acoustic pressure in Pa and vector particle velocity in m·s^{-1}, respectively; both are functions of spatial coordinates $\mathbf{x} = [x_1, x_2, x_3] \in \mathbb{R}^3$ and time $t \geq 0$. ∇ and $\nabla\cdot$ represent the three-dimensional gradient and divergence operations, respectively. c is the wave speed, in m·s^{-1}, and ρ is density, in kg·m^{-3}; both are assumed constant here. From these constants, the acoustic impedance and admittance of air may be defined as

$$Z_0 \triangleq \rho c, \quad Y_0 \triangleq 1/Z_0 = 1/\rho c. \tag{2}$$

A. Immersed boundary

The immersed boundary formulation presented in the 1D case in the companion paper[26] may be extended directly to 3D in the following way. Suppose that an immersed boundary, assumed infinitely thin, is defined over a two-dimensional orientable surface $\Omega \subset \mathbb{R}^3$. See Fig. 1 (left). With each $\boldsymbol{\xi} \in \Omega$ is associated a normal vector $\mathbf{n}(\boldsymbol{\xi})$. The immersed boundary formulation is now

$$\begin{aligned}&\frac{1}{\rho c^2}\partial_t p + \nabla\cdot\mathbf{v} + \iint_\Omega v_\Delta(\boldsymbol{\xi},t)\delta^{(3)}(\mathbf{x}-\boldsymbol{\xi})d\boldsymbol{\xi} = \delta^{(3)}(\mathbf{x}-\mathbf{x}_s)u,\\ &\rho\partial_t\mathbf{v} + \nabla p + \iint_\Omega p_\Delta(\boldsymbol{\xi},t)\mathbf{n}(\boldsymbol{\xi})\delta^{(3)}(\mathbf{x}-\boldsymbol{\xi})d\boldsymbol{\xi} = \mathbf{0}.\end{aligned} \tag{3}$$

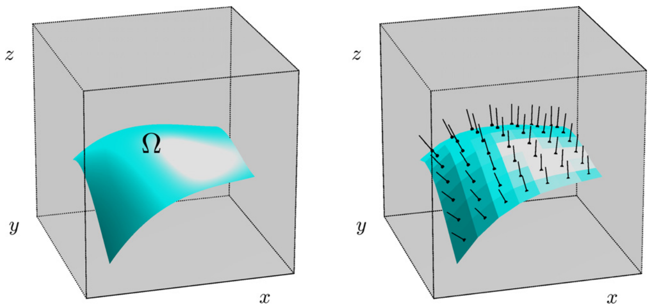

FIG. 1. (Color online) (Left) A surface Ω embedded in $\mathbb{R}^3$. (Right) Subdivision into K flat patches, with surface areas $S^{(k)}$, at coordinates $\boldsymbol{\xi}^{(k)}$, indicated by dots, and normal vectors $\mathbf{n}^{(k)}$ indicated by lines, for $k = 1, \ldots, K$.

An external source term, of strength $u(t)$ in m^3·s^{-1} is included and acts pointwise at location $\mathbf{x} = \mathbf{x}_s$. $\delta^{(3)}$ represents a three-dimensional Dirac delta function. Initial conditions are assumed to be quiescent. Note that (3) is more general than other formulations employed for the same system[21,27] due to the presence of v_Δ.

Here, the scalar driving terms $p_\Delta(\boldsymbol{\xi}, t)$ and $v_\Delta(\boldsymbol{\xi}, t)$ are defined for $\boldsymbol{\xi} \in \Omega$. The associated field variables upon which they depend are written as $\bar{p}(\boldsymbol{\xi}, t)$ and $\bar{v}(\boldsymbol{\xi}, t)$,

$$\bar{p}(\boldsymbol{\xi}, t) = \iiint_{\mathbb{R}^3} p(\mathbf{x}, t)\delta^{(3)}(\mathbf{x} - \boldsymbol{\xi})d\mathbf{x}, \tag{4a}$$

$$\bar{v}(\boldsymbol{\xi}, t) = \mathbf{n}(\boldsymbol{\xi}) \cdot \iiint_{\mathbb{R}^3} \mathbf{v}(\mathbf{x}, t)\delta^{(3)}(\mathbf{x} - \boldsymbol{\xi})d\mathbf{x}. \tag{4b}$$

Define the Laplace transform $\hat{f}(\boldsymbol{\xi}, s)$ of $f(\boldsymbol{\xi}, t)$, $\boldsymbol{\xi} \in \Omega$ as

$$\hat{f}(\boldsymbol{\xi}, s) = \int_0^\infty f(\boldsymbol{\xi}, t)e^{-st}dt, \tag{5}$$

where s is a complex frequency variable. The relationships between driving functions p_Δ, v_Δ and field variables $\bar{p}$, $\bar{v}$ can be expressed, in the Laplace domain, as

$$\hat{p}_\Delta(\boldsymbol{\xi}, s) = 2Z_0 z_v(\boldsymbol{\xi}, s)\hat{\bar{v}}(\boldsymbol{\xi}, s), \tag{6a}$$

$$\hat{v}_\Delta(\boldsymbol{\xi}, s) = 2Y_0 y_p(\boldsymbol{\xi}, s)\hat{\bar{p}}(\boldsymbol{\xi}, s), \tag{6b}$$

for nondimensional impedance $z_v(\boldsymbol{\xi}, s)$ and admittance $y_p(\boldsymbol{\xi}, s)$ distributions defined over $\boldsymbol{\xi} \in \Omega$. (The additional factors of 2 are employed here to simplify subsequent calculations, as in the 1D case.[26])

B. Positive realness of immittances and special cases

A function $w(s)$ of a complex variable s is called positive real[29] if it satisfies

$$\mathrm{Re}(w(s)) \geq 0 \quad \text{when} \quad \mathrm{Re}(s) \geq 0, \tag{7a}$$

$$\mathrm{Im}(w(s)) = 0 \quad \text{when} \quad \mathrm{Im}(s) = 0. \tag{7b}$$

Positive real functions are constrained to be rational according to some definitions,[29] so that

$$w(s) = \frac{\sum_{\nu=0}^{P} \eta_\nu s^\nu}{\sum_{\nu=0}^{Q} \zeta_\nu s^\nu} \tag{8}$$

for some coefficients η_ν, $\nu = 0, \ldots, P$ and ζ_ν, $\nu = 0, \ldots, Q$. A flexible special case of interest in acoustics is the form

$$w(s) = \alpha + \beta s + \gamma/s, \tag{9}$$

which is positive real for $\alpha, \beta, \gamma \geq 0$.

Both $y_p(\xi, s)$ and $z_v(\xi, s)$ are assumed to be positive real pointwise, for all $\boldsymbol{\xi} \in \Omega$, although their forms can vary with location over Ω. As in the one-dimensional case,[26] if

$$y_p(\boldsymbol{\xi}, s) = 0 \quad \forall \boldsymbol{\xi} \in \Omega, \tag{10}$$

then the boundary is of non-porous type. If

$$z_v(\boldsymbol{\xi}, s) = 1/y_p(\boldsymbol{\xi}, s) \quad \forall \boldsymbol{\xi} \in \Omega, \tag{11}$$

then the surface acts as an impedance boundary with no transmission and of surface impedance $z_v(\boldsymbol{\xi}, s)$.

C. Reduction over a surface mesh

As a preparatory step to discretisation, the driving terms in system (3) must be approximated by sums of a finite number of driving terms. Suppose that Ω is decomposed into K non-overlapping subdomains $\Omega^{(k)}$, $k = 1, \ldots, K$. Each subdomain is centered at coordinates $\boldsymbol{\xi}^{(k)}$, with surface area $S^{(k)} = |\Omega^{(k)}|$. The resolution of the subdomains is assumed sufficiently fine that each $\Omega^{(k)}$ is effectively flat (while not larger than the grid spacing), with normal vector $\mathbf{n}^{(k)}$. (Note that the formalism presented below is insensitive to the choice of either $\mathbf{n}^{(k)}$ or $-\mathbf{n}^{(k)}$.) See Fig. 1 (right). System (3) may then be approximated as

$$\begin{aligned}&\frac{1}{\rho c^2}\partial_t p + \nabla \cdot \mathbf{v} + \sum_{k=1}^{K} v_\Delta^{(k)}\delta^{(3)}(\mathbf{x} - \boldsymbol{\xi}^{(k)})S^{(k)} \\ &\quad = \delta^{(3)}(\mathbf{x} - \mathbf{x}_s)u, \\ &\rho\partial_t \mathbf{v} + \nabla p + \sum_{k=1}^{K} p_\Delta^{(k)}\mathbf{n}^{(k)}\delta^{(3)}(\mathbf{x} - \boldsymbol{\xi}^{(k)})S^{(k)} = \mathbf{0}.\end{aligned} \tag{12a}$$

Here, $v_\Delta^{(k)}(t)$ and $p_\Delta^{(k)}(t)$, $k = 1, \ldots, K$ are scalar driving functions. They are related to interpolated field values $\bar{p}^{(k)}(t)$ and $\bar{v}^{(k)}(t)$ by an approximation to (4) as

$$\begin{aligned}\bar{p}^{(k)}(t) &= \iiint_{\mathbb{R}^3} p(\mathbf{x}, t)\delta^{(3)}(\mathbf{x} - \boldsymbol{\xi}^{(k)})d\mathbf{x}, \\ \bar{v}^{(k)}(t) &= \mathbf{n}^{(k)} \cdot \iiint_{\mathbb{R}^3} \mathbf{v}(\mathbf{x}, t)\delta^{(3)}(\mathbf{x} - \boldsymbol{\xi}^{(k)})d\mathbf{x}.\end{aligned} \tag{12b}$$

Finally, the relationships (6) are approximated as

$$\begin{aligned}\hat{p}_\Delta^{(k)}(s) &= 2Z_0 z_v^{(k)}(s)\hat{\bar{v}}^{(k)}(s), \\ \hat{v}_\Delta^{(k)}(s) &= 2Y_0 y_p^{(k)}(s)\hat{\bar{p}}^{(k)}(s).\end{aligned} \tag{12c}$$

Here, $z_v^{(k)}(s)$ and $y_p^{(k)}(s)$ are the immittances associated with the kth surface patch, $k = 1, \ldots, K$. Both are assumed to be positive real rational functions, of the form

$$z_v^{(k)}(s) = \frac{\sum_{\nu=0}^{P_v^{(k)}} \eta_{v,\nu}^{(k)} s^\nu}{\sum_{\nu=0}^{Q_v^{(k)}} \zeta_{v,\nu}^{(k)} s^\nu}, \quad y_p^{(k)}(s) = \frac{\sum_{\nu=0}^{P_p^{(k)}} \eta_{p,\nu}^{(k)} s^\nu}{\sum_{\nu=0}^{Q_p^{(k)}} \zeta_{p,\nu}^{(k)} s^\nu}, \tag{13}$$

with associated coefficients $\eta_{v,\nu}^{(k)}$, $\nu = 0, \ldots, P_v^{(k)}$, $\zeta_{v,\nu}^{(k)}$, $\nu = 0, \ldots, Q_v^{(k)}$, $\eta_{p,\nu}^{(k)}$, $\nu = 0, \ldots, P_p^{(k)}$, and $\zeta_{p,\nu}^{(k)}$, $\nu = 0, \ldots, Q_p^{(k)}$, for $k = 1,\ldots,K$. Notice in particular that the coefficients and even orders of the polynomials in the rational functions above can vary with the surface patch index k, meaning that the character of the immersed boundary can vary from one point to another. System (12), alongside definitions (13), is the point of departure for time domain simulation.

III. FDTD METHOD

The development of FDTD methods in 3D closely follows the 1D case[26] and is presented in brief here, using the system (1) in free space as a starting point.

Interleaved time domain methods are commonly used to simulate the first-order system (1) directly.[1,2] A starting point is the definition of a grid function $p_{\mathbf{l}}^n$, for integer $n \geq 0$ and integer-valued vector $\mathbf{l} \in \mathbb{Z}^3$, intended to approximate $p(\mathbf{x}, t)$ at $\mathbf{x} = \mathbf{l}X$ and $t = nT$, where X is the grid spacing in m, and T is the time step in s. An interleaved grid function $\mathbf{v}_{\mathbf{l}}^{n+1/2} = [v_{1,\mathbf{l}}^{n+1/2}, v_{2,\mathbf{l}}^{n+1/2}, v_{3,\mathbf{l}}^{n+1/2}]$, again for integer-valued 3-vectors $\mathbf{l}$, approximates the velocity. Despite the uniform spatial indexing, used here for simplicity, the three components $v_{\mu,\mathbf{l}}^{n+1/2}$, $\mu = 1, 2, 3$ are not co-located; rather, $v_{\mu,\mathbf{l}}^{n+1/2}$ represents an approximation to $v_\mu(\mathbf{x}, t)$ at $t = (n + 1/2)T$ and $\mathbf{x} = (\mathbf{l} - (1/2)\mathbf{e}_\mu)X$, where $\mathbf{e}_\mu$ is a unit vector in direction x_μ. See Fig. 2.

Time difference operators are as defined in the 1D case.[26] For a grid function $f_{\mathbf{l}}^n$, the difference operators $D_t^{\pm}$ and averaging operators $M_t^{\pm}$ are defined as

$$D_t^{\pm} f_{\mathbf{l}}^n = \pm\left(f_{\mathbf{l}}^{n\pm1} - f_{\mathbf{l}}^n\right), \quad M_t^{\pm} f_{\mathbf{l}}^n = \frac{1}{2}\left(f_{\mathbf{l}}^{n\pm1} + f_{\mathbf{l}}^n\right). \tag{14}$$

$(1/T)D_t^{\pm}$ is an approximation to ∂_t and holds equally when applied to a grid function defined at interleaved time steps $n + 1/2$. Basic spatial difference operators may be defined, with reference to a grid function $f_{\mathbf{l}}^n$, as

$$D_{\mu}^{\pm} f_{\mathbf{l}}^n = \pm\left(f_{\mathbf{l}\pm\mathbf{e}_\mu}^n - f_{\mathbf{l}}^n\right), \quad \mu = 1, 2, 3. \tag{15}$$

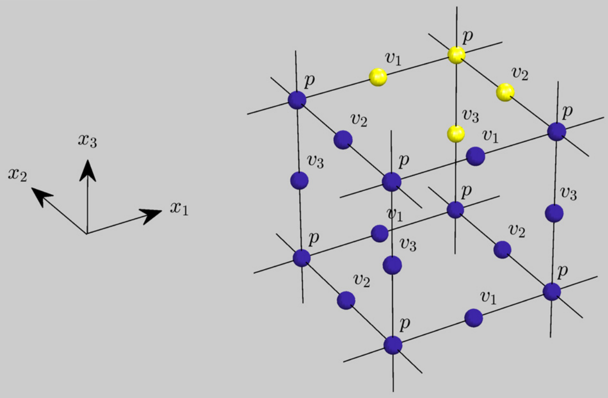

FIG. 2. (Color online) Interleaved computational grid, showing the locations of pressure grid function $p_{\mathbf{l}}^n$ and the components of the particle velocity $\mathbf{v}_{\mathbf{l}}^{n+1/2}$ separately. Those grid points with a common index $\mathbf{l}$ are indicated in yellow.

This definition holds similarly when applied to a time interleaved grid function $f_{\mathbf{l}}^{n+1/2}$. Approximations $D^{\pm}$ to the gradient ∇ follow as

$$D^{\pm} = \left[D_1^{\pm}, D_2^{\pm}, D_3^{\pm}\right]. \tag{16}$$

A basic FDTD scheme for (1), describing the free field problem, then follows as

$$\frac{1}{\rho c^2 T} D_t^+ p_{\mathbf{l}}^n + \frac{1}{X} D^+ \cdot \mathbf{v}_{\mathbf{l}}^{n+1/2} = 0, \tag{17a}$$

$$\frac{\rho}{T} D_t^- \mathbf{v}_{\mathbf{l}}^{n+1/2} + \frac{1}{X} D^- p_{\mathbf{l}}^n = \mathbf{0}. \tag{17b}$$

At this stage, it is useful to constrain the computational domain of the problem to be finite. Suppose that N_p and N_v are the total numbers of grid points required to represent the pressure grid values $p_{\mathbf{l}}^n$ and all components of the velocity $\mathbf{v}_{\mathbf{l}}^{n+1/2}$. Then we may define the consolidated vectors $\mathbf{p}^n$ and $\mathbf{v}^{n+1/2}$, of sizes $N_p \times 1$ and $N_v \times 1$, respectively. (The most direct way to do this, given a grid function indexed over a parallelepipedal volume, is to extract consecutive 1D vectors in one dimension across regular indexing in the two remaining dimensions. All such orderings lead to equivalent results.) The discrete divergence operation $D^+\cdot$ and gradient operation D^- can be represented as matrices $\mathbf{D}^+$ and $\mathbf{D}^-$, of sizes $N_p \times N_v$ and $N_v \times N_p$, respectively. Furthermore, it is often the case that $\mathbf{D}^- = -(\mathbf{D}^+)^\top$, as, e.g., under Neumann or periodic conditions over the domain boundary. As the focus here is on the immersed boundary method and the problem interior, this property will be assumed to hold here. Thus, the scheme (17) may be written in vector-matrix form as

$$\begin{aligned} &D_t^+ \mathbf{p}^n + Z_0 \lambda \mathbf{D}^+ \mathbf{v}^{n+1/2} = \mathbf{0}, \\ &D_t^- \mathbf{v}^{n+1/2} + Y_0 \lambda \mathbf{D}^- \mathbf{p}^n = \mathbf{0}. \end{aligned} \tag{18}$$

Note the appearance of the characteristic impedance Z_0 and admittance Y_0 as defined in (2), as well as the Courant number λ, defined as $\lambda = cT/X$. For this scheme, the numerical stability condition is

$$\lambda \leq 1/\sqrt{3}. \tag{19}$$

A. Approximations to the three-dimensional Dirac delta function and matrix representations

Instances of the three-dimensional Dirac delta function appear in both (12a) as a driving term and (12b) as an interpolant. Approximations are, thus, required over four distinct grids, for the four components of p and $\mathbf{v}$, at the locations $\boldsymbol{\xi}^{(k)} = [\xi_1^{(k)}, \xi_2^{(k)}, \xi_3^{(k)}]$, $k = 1,\ldots,K$. Over the pressure grid (see Fig. 2), the approximation will be of the form of a grid function $j_{p,l}(\boldsymbol{\xi}^{(k)})$, where

$$\frac{1}{X^3} j_{p,\mathbf{l}}(\boldsymbol{\xi}^{(k)}) \approxeq \delta^{(3)}(\mathbf{x} - \boldsymbol{\xi}^{(k)}), \quad k = 1,\ldots,K. \tag{20}$$

Similarly to the 1D case,[26] a factor of $1/X^3$ has been extracted so that, to correspond to an approximation to a Dirac delta function, a minimum requirement (or moment condition) is that the elements of $j_{p,\mathbf{l}}$ sum to unity. It is simplest to construct such approximations as Cartesian products of 1D approximations to the Dirac delta function $j_{p,l_\mu}(\xi^{(k)}_\mu)$, $\mu = 1, 2, 3$, such as those described in detail in the companion paper,[26] so that

$$j_{p,\mathbf{l}}(\boldsymbol{\xi}^{(k)}) = j_{p,l_1}(\xi^{(k)}_1) j_{p,l_2}(\xi^{(k)}_2) j_{p,l_3}(\xi^{(k)}_3). \tag{21}$$

Examples are the raised cosine distribution,[30] heavily used in immersed boundary applications, and polynomial interpolants, including the triangular distribution.[18,23] Other non-separable designs are available in 3D and can have superior performance, although they require a more involved design procedure.[31] Following from the vector-matrix representation described above in Sec. III, the approximation to the kth Dirac delta function over the pressure grid may be represented as an $N_p \times 1$ vector $\mathbf{j}^{(k)}_p$, according to the reordering described above in Sec. III. All K such vectors may be arranged in an $N_p \times K$ matrix $\mathbf{J}_p = [\mathbf{j}^{(1)}_p, \ldots, \mathbf{j}^{(K)}_p]$. See the companion paper[26] for more on the 1D construction of these vectors.

Similarly, approximations to the Dirac delta functions may be constructed over the three distinct grids for the velocity components (see Fig. 2), giving, for the kth Dirac delta function, $k = 1, \ldots, K$, the three approximants $\mathbf{j}^{(k)}_{v,\mu}$, $\mu = 1, 2, 3$. From these, and incorporating the components of the normal vectors $\mathbf{n}^{(k)} = [n^{(k)}_1, n^{(k)}_2, n^{(k)}_3]$, one may construct the $N_v \times K$ matrix $\mathbf{N}_v$ as

$$\mathbf{N}_v = \begin{bmatrix} n^{(1)}_1 \mathbf{j}^{(1)}_{v,1} & \cdots & n^{(K)}_1 \mathbf{j}^{(K)}_{v,1} \\ n^{(1)}_2 \mathbf{j}^{(1)}_{v,2} & \cdots & n^{(K)}_2 \mathbf{j}^{(K)}_{v,2} \\ n^{(1)}_3 \mathbf{j}^{(1)}_{v,3} & \cdots & n^{(K)}_3 \mathbf{j}^{(K)}_{v,3} \end{bmatrix}. \tag{22}$$

It is also useful to introduce the $K \times K$ diagonal matrix $\mathbf{S}$, the diagonal elements of which are defined as

$$[\mathbf{S}]_{kk} = S^{(k)}/X^2, \quad k = 1, \ldots, K, \tag{23}$$

consisting of the patch areas $S^{(k)}$ scaled against the square of the grid spacing X. These values give a simple measure of the density of the driving terms relative to the underlying three-dimensional grid for the acoustic field.

Finally, an approximation to the Dirac delta function employed to drive the system at coordinates $\mathbf{x} = \mathbf{x}_s$ in (12a) may be constructed as the $N_p \times 1$ vector $\mathbf{j}_s$.

B. Immersed boundary immittances

Discretisation of a single immersed boundary driving term has been dealt with in the companion article.[26] The present case of discretisation of a collection of such terms as in system (12) follows immediately, as the individual driving terms $p^{(k)}_\Delta$, $v^{(k)}_\Delta$ are related pointwise to the interpolated field values $\bar{v}^{(k)}$, $\bar{p}^{(k)}$, through (12c). Consider the immittance definitions in (13). When transformed to the time domain, and under zero initial conditions, the following ordinary differential equations result:

$$\sum_{\nu=0}^{Q^{(k)}_v} \zeta^{(k)}_{v,\nu} \frac{d^\nu}{dt^\nu} p^{(k)}_\Delta = 2Z_0 \sum_{\nu=0}^{P^{(k)}_v} \eta^{(k)}_{v,\nu} \frac{d^\nu}{dt^\nu} \bar{v}^{(k)}, \tag{24a}$$

$$\sum_{\nu=0}^{Q^{(k)}_p} \zeta^{(k)}_{p,\nu} \frac{d^\nu}{dt^\nu} v^{(k)}_\Delta = 2Y_0 \sum_{\nu=0}^{P^{(k)}_p} \eta^{(k)}_{p,\nu} \frac{d^\nu}{dt^\nu} \bar{p}^{(k)}, \tag{24b}$$

for $k = 1, \ldots, K$. Under trapezoidal numerical integration, through the substitution $d/dt \rightarrow (1/T)D^{\bigcirc}_t$, where

$$D^{\bigcirc}_t = (M^+_t)^{-1} D^+_t = (M^-_t)^{-1} D^-_t, \tag{25}$$

and $M^\pm_t$ are as defined in (14), these ODEs become

$$\begin{aligned} \sum_{\nu=0}^{Q^{(k)}_v} \frac{\zeta^{(k)}_{v,\nu} (D^{\bigcirc}_t)^\nu}{T^\nu} p^{(k),n+1/2}_\Delta &= 2Z_0 \sum_{\nu=0}^{P^{(k)}_v} \frac{\eta^{(k)}_{v,\nu} (D^{\bigcirc}_t)^\nu}{T^\nu} \bar{v}^{(k),n+1/2}, \\ \sum_{\nu=0}^{Q^{(k)}_p} \frac{\zeta^{(k)}_{p,\nu} (D^{\bigcirc}_t)^\nu}{T^\nu} v^{(k),n}_\Delta &= 2Y_0 \sum_{\nu=0}^{P^{(k)}_p} \frac{\eta^{(k)}_{p,\nu} (D^{\bigcirc}_t)^\nu}{T^\nu} \bar{p}^{(k),n}. \end{aligned} \tag{26}$$

Ultimately, as in the 1D case as described in the companion paper,[26] the following relations may be derived:

$$\begin{aligned} p^{(k),n+1/2}_\Delta &= Z_0 \gamma^{(k)}_v \bar{v}^{(k),n+1/2} + q^{(k),n-1/2}_v, \\ v^{(k),n}_\Delta &= Y_0 \gamma^{(k)}_p \bar{p}^{(k),n} + q^{(k),n-1}_p. \end{aligned} \tag{27}$$

Here, for positive real immittances, $\gamma^{(k)}_v$ and $\gamma^{(k)}_p$, $k = 1, \ldots, K$ are non-negative constants, and $q^{(k),n-1/2}_v$ and $q^{(k),n-1}_p$ contain previously computed values of the interpolated field values and jumps at the K driving locations.

C. Complete scheme

Introduce now the $K \times 1$ vectors $\bar{\mathbf{p}}^n$ and $\bar{\mathbf{v}}^{n+1/2}$, representing interpolated field values, and $\mathbf{p}^{n+1/2}_\Delta$ and $\mathbf{v}^n_\Delta$, representing pressure and normal velocity jumps across the surface Ω at the driving locations. The complete scheme approximating (12) may be written in a compact vector-matrix form. For (12a), one has

$$\begin{aligned} D^+_t \mathbf{p}^n + Z_0 \lambda \left(\mathbf{D}^+ \mathbf{v}^{n+1/2} + \mathbf{J}_p \mathbf{S} M^+_t \mathbf{v}^n_\Delta \right) &= \frac{Z_0 \lambda}{X^2} \mathbf{j}_s M^+_t u^n, \\ D^-_t \mathbf{v}^{n+1/2} + Y_0 \lambda \left(\mathbf{D}^- \mathbf{p}^n + \mathbf{N}_v \mathbf{S} M^-_t \mathbf{p}^{n+1/2}_\Delta \right) &= \mathbf{0}. \end{aligned} \tag{28a}$$

The use of the averaging operators $M^\pm_t$ above, defined earlier in (14), serves to center the approximations, leading to second-order accuracy—it is also crucial to the analysis of numerical stability, as explained in detail in the Appendix. Equation (12b) may be approximated as

$$\bar{\mathbf{p}}^n = \mathbf{J}^\top_p \mathbf{p}^n, \quad \bar{\mathbf{v}}^{n+1/2} = \mathbf{N}^\top_v \mathbf{v}^{n+1/2}. \tag{28b}$$

Finally, the immittance relationships in (27) can be written as

$$\mathbf{p}_{\Delta}^{n+1/2} = Z_0\boldsymbol{\Gamma}_v\bar{\mathbf{v}}^{n+1/2} + \mathbf{q}_v^{n-1/2}, \quad \mathbf{v}_{\Delta}^{n} = Y_0\boldsymbol{\Gamma}_p\bar{\mathbf{p}}^{n} + \mathbf{q}_p^{n-1}. \tag{28c}$$

Here, $\boldsymbol{\Gamma}_v$ and $\boldsymbol{\Gamma}_p$ are diagonal $K \times K$ matrices containing the coefficients $\gamma_v^{(k)}$ and $\gamma_p^{(k)}$, $k = 1, \ldots, K$ on their respective diagonals. The values $q_v^{(k),n-1/2}$ and $q_p^{(k),n-1}$ have been consolidated into the $K \times 1$ vectors $\mathbf{q}_v^{n-1/2}$ and $\mathbf{q}_p^{n-1}$, respectively.

As in the 1D case,[26] the scheme (28) may be reduced to a pair of updates as

$$\begin{aligned}\mathbf{A}_p\mathbf{p}^{n+1} &= \mathbf{B}_p\mathbf{p}^{n} - Z_0\lambda\mathbf{D}^{+}\mathbf{v}^{n+1/2} \\ &\quad - Z_0\lambda\mathbf{J}_p\mathbf{S}M_t^{+}\mathbf{q}_p^{n-1} + \frac{Z_0\lambda}{X^2}\mathbf{j}_s u^n,\end{aligned} \tag{29a}$$

$$\begin{aligned}\mathbf{A}_v\mathbf{v}^{n+1/2} &= \mathbf{B}_v\mathbf{v}^{n-1/2} - Y_0\lambda\mathbf{D}^{-}\mathbf{p}^{n} \\ &\quad - Y_0\lambda\mathbf{N}_v\mathbf{S}M_t^{-}\mathbf{q}_v^{n-1/2}.\end{aligned} \tag{29b}$$

Defining the $N_p \times K$ matrix $\mathbf{W}_p = \sqrt{\lambda/2}\mathbf{J}_p\mathbf{S}^{1/2}\boldsymbol{\Gamma}_p^{1/2}$ and the $N_v \times K$ matrix $\mathbf{W}_v = \sqrt{\lambda/2}\mathbf{N}_v\mathbf{S}^{1/2}\boldsymbol{\Gamma}_v^{1/2}$, one has, for the matrices $\mathbf{A}_p$, $\mathbf{B}_p$ in (29),

$$\mathbf{A}_p = \mathbf{I}_{N_p} + \mathbf{W}_p\mathbf{W}_p^{\top}, \quad \mathbf{B}_p = \mathbf{I}_{N_p} - \mathbf{W}_p\mathbf{W}_p^{\top}. \tag{30}$$

This is of the form the identity plus a rank-K perturbation. The Woodbury identity[32] may be employed to arrive at an explicit inverse for $\mathbf{A}_p$,

$$\mathbf{A}_p^{-1} = \mathbf{I}_{N_p} - \mathbf{W}_p\left(\mathbf{I}_K + \mathbf{W}_p^{\top}\mathbf{W}_p\right)^{-1}\mathbf{W}_p^{\top}. \tag{31}$$

Thus, a $K \times K$ linear system solution is required. A similar argument follows for the construction of $\mathbf{A}_v$ and $\mathbf{B}_v$. Notice, however, that, for local Dirac delta function approximations, $\mathbf{W}_p$ and $\mathbf{W}_v$ will in general be sparse, and, thus, sparse matrix inversion methods may be useful.[33]

The determination of numerical stability conditions for the scheme (28) is more involved than in the case of impedance boundary termination for FDTD or FVTD methods[15] or for immersed boundaries where only a driving term p_Δ is present[27]—the usual case in immersed boundary methods. It can be accomplished in the Laplace domain in discrete time to determine bounds on system poles such that solutions are non-increasing. In the present case, the standard CFL condition (19) is very nearly recovered (without the case of equality, which is unimportant in practice) and is unaffected by the inclusion of the immersed boundary. See the Appendix.

IV. NUMERICAL RESULTS

All simulations are run using the scheme (29), using $c = 344\,\mathrm{m{\cdot}s^{-1}}$ and $\rho = 1.18\ \mathrm{kg{\cdot}m^{-3}}$, and with a time step of $T = 2 \times 10^{-5}$ s. The Courant number was chosen as close to the bound (19) as possible (here, $\lambda = 0.5754$). The computational domain is a cube of side length 2.2 m, with first-order absorbing boundary conditions[34] employed. In all examples, the ratio of the surface patch area to X^2 is near 1, and approximations to the Dirac delta function are of fifth-order Lagrangian type.[26] The source term u^n is Gaussian, with effective 60 dB bandwidth[26] f_{60} in Hz and maximum amplitude 10^{-3} $\mathrm{m^3{\cdot}s}$.

A. Square barrier

Consider first a square barrier, of side length 1 m and nominally oriented with the x_3 axis, so that $\mathbf{n} = [0, 0, 1]$. The immittances z_v and y_m are assumed frequency-dependent but constant over the barrier surface. Patches are square-shaped, with the patch side length subdividing the barrier side length evenly. In Fig. 3, snapshots of the time evolution of the acoustic field are shown, where the source location is $\mathbf{x}_s = (0, 0, 0.3)$ m. Here, the immittances are chosen as $y_p(s) = 1/w(s)$, $z_v(s) = w(s)$, uniformly over the barrier, where $w(s)$ is as defined in (9) in terms of the parameters α, β, and γ. This corresponds to an impedance boundary condition, with no transmission. Four cases are shown, illustrating different impedance boundary condition types: resistive, inertial, stiff, and resonant, with both mass and stiffness effects. Faintly visible in the latter three cases are leakage effects. As in the 1D case,[26] the amount of leakage depends on the bandwidth of the excitation; in this case, a high bandwidth excitation of $f_{60} = 4$ kHz has been chosen to exhibit this effect.

As a further illustration, consider again the resonant impedance boundary condition, now under the more realistic use case of different orientations of the barrier relative to the Cartesian grid. See Fig. 4. Notice that the leakage, still faintly visible, exhibits a dependence on the rotation of the barrier. There is, thus, clearly an interaction between the direction-dependent numerical dispersion of the FDTD scheme[35] and the immersed boundary.

Alongside these qualitative illustrations, it is useful to perform comparisons against a known solution. While exact solutions are difficult to obtain in the present case of an impedance boundary condition over a barrier of finite size, it is possible to compare results against solutions obtained using a more basic FDTD discretisation over a cube, with an impedance boundary over one face.[4] Thus, the solutions should match, over the interval preceding the arrival of waves diffracting around the barrier, as is easily visible in Fig. 3. See Fig. 5 (left), illustrating a source/receiver configuration, with a single source, located directly above the immersed boundary center, and three outputs taken, labeled A, B, and C: Points A and B are located on the same side of the barrier as the source, and point C is on the opposite side of the immersed boundary and is intended to capture spurious leakage in this case of an impedance boundary condition. Comparisons are shown with the reference solution, calculated with a time step of $T = 5 \times 10^{-6}$ s, for three different orientations of the immersed boundary with respect to

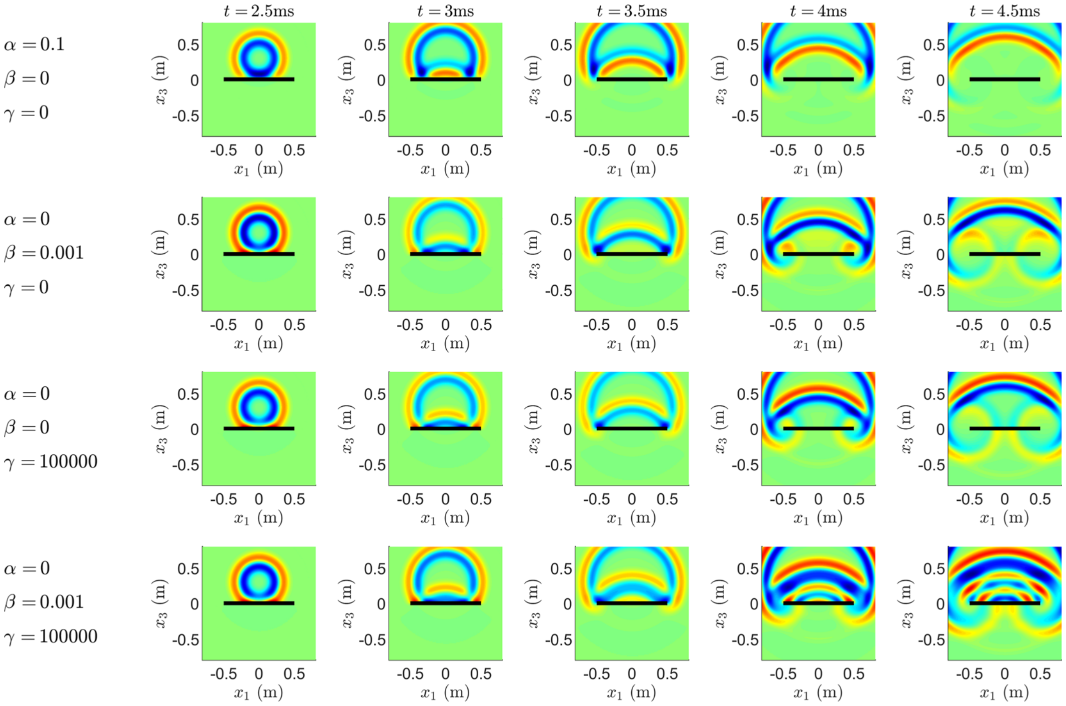

FIG. 3. (Color online) Time evolution of the acoustic field, for an immersed boundary operating as an impedance boundary condition, and over a square region of side length 1 m, oriented with the positive x_3, and centered at $x_1 = x_2 = x_3 = 0$. Snapshots are shown in the (x_1, x_3) plane, for different choices of immittance parameters as indicated in each row. Here, and in subsequent figures, red/blue colorings correspond to high and low pressures, respectively, scaled to their maximum values for a given snapshot. The barrier cross section, of infinitesimal thickness, is indicated as a black line.

the Cartesian axes. In all cases, the match is very good; spurious leakage at point C is small and highly dependent on the orientation of the immersed boundary, confirming intuitions drawn from the examination of Fig. 4.

Finally, results in Fig. 6 are shown, under conditions similar to those in Fig. 3 for z_v, but now under the condition that $y_p = 0$, corresponding to a barrier with no normal velocity jump across it and capable of transmitting energy, as described in the comapnion paper.[26]

B. Spherical barrier

One use of wave-based acoustic simulation methods, such as FDTD, is the simulation of head-related impulse

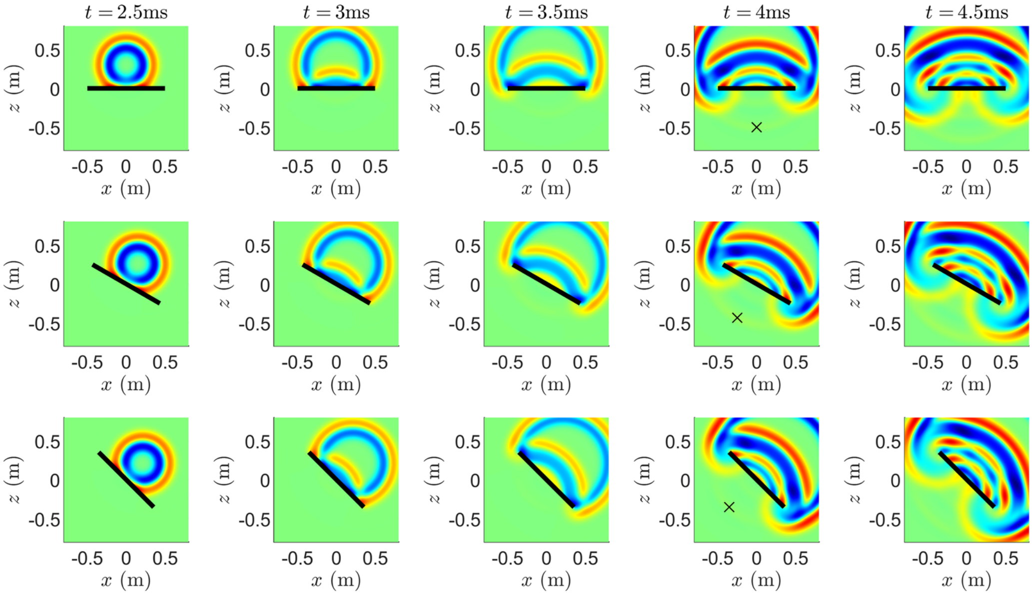

FIG. 4. (Color online) Time evolution of the acoustic field, for an immersed boundary operating as an impedance boundary condition, and over a square region of side length 1 m, under different orientations: unrotated (top row) and rotated by $\pi/6$ (middle row) and $\pi/4$ (bottom row) radians about the x_2 axis. The impedance boundary is of the resonant type as shown in the last row of Fig. 3. The barrier cross section, of infinitesimal thickness, is indicated as a black line. Locations where spurious leakage through this immersed boundary are visible, indicated by crosses.

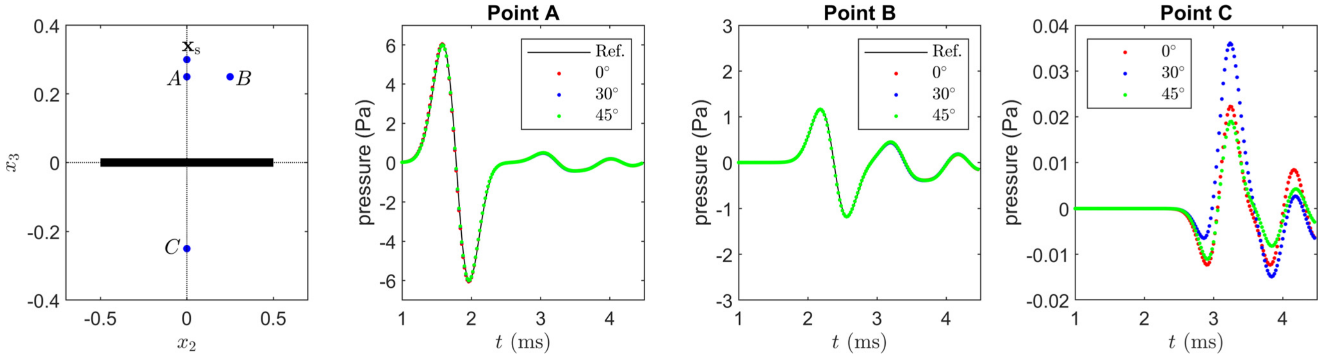

FIG. 5. (Color online) (Left) Immersed boundary configuration, for an infinitesimally thin square barrier of side length 1 m, oriented with the x_3 axis, and shown in cross section (a black line) in the (x_2, x_3) plane. The source location $\mathbf{x}_s$ is indicated, as well as output coordinates at A, B, and C. Outputs at points A, B, and C are plotted in their respective panels, for different rotations of the immersed boundary with respect to the Cartesian axes. In the case of points A and B, a reference solution is also plotted. Outputs at point C illustrate spurious leakage through the immersed boundary.

responses and transfer functions, given a known head geometry. This can be very challenging, due to the irregularity of this geometry.[11] The spherical barrier is a useful simplified test case in the context of the modeling of diffraction around the human head.[36] In previous work, an immersed boundary emulating a rigid boundary condition over a sphere was demonstrated.[27] Here, however, it is shown that the model can be generalised to include any impedance over the surface of the sphere.[37]

Consider a sphere, of radius R m, centered at $\mathbf{x} = \mathbf{0}$. Assume an exterior problem setting. A family of well-known boundary conditions can be written as

$$p + Z_0 \alpha v_n = 0 \quad \text{over} \quad |\mathbf{x}| = R, \tag{32}$$

where $v_n = \mathbf{v} \cdot \mathbf{x}/|\mathbf{x}|$ is the outward normal component of the velocity over the sphere and for constant $\alpha \geq 0$. When $\alpha = +\infty$, a rigid or Neumann condition results. When $\alpha = 0$, the sphere is referred to as of the "pressure release" type. In general, the condition above is resistive.

In Fig. 7, plots of the time evolution of the acoustic field are shown, for a sphere with $R = 0.25$ m. An immersed boundary is used, with $z_v = 1/y_p = \alpha$, corresponding to an impedance boundary condition. The ratio of the patch area to X^2 is approximately 1, and a spiral-based sampling method[38] is used to tesselate the sphere surface—patch areas are, to a very high degree of accuracy, the total surface area of the sphere divided by the number of patches. The source, with $f_{60} = 4$ kHz, is located at $\mathbf{x}_s = (0,\ 0,\ 0.4)$ m. Results are shown for the rigid, pressure

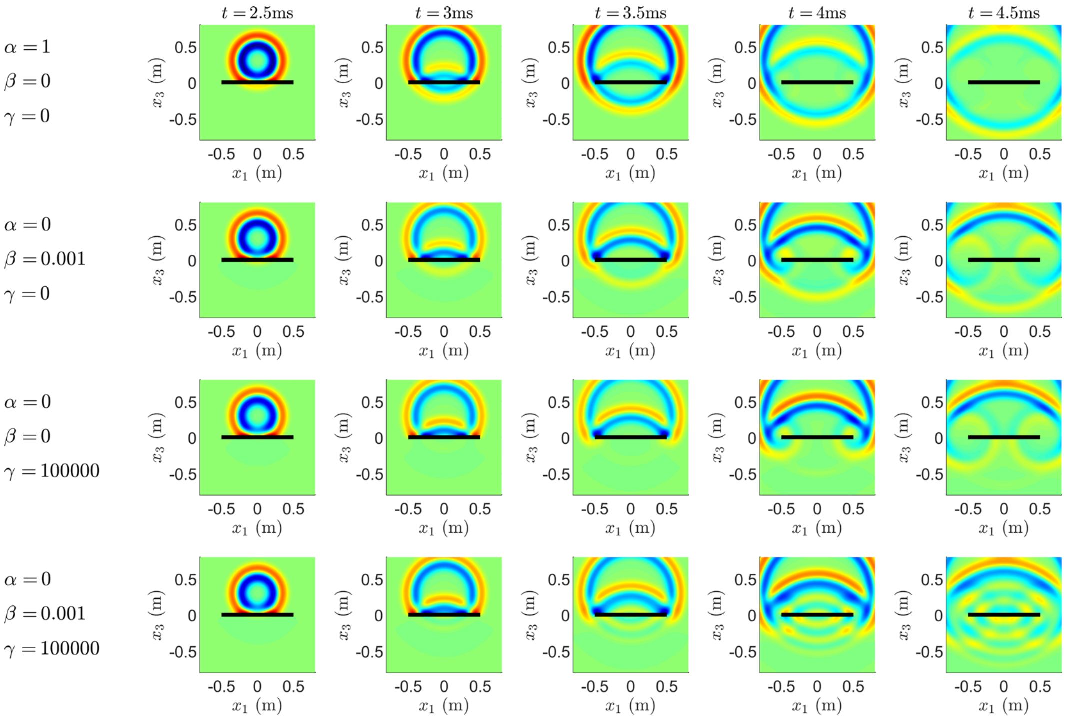

FIG. 6. (Color online) Time evolution of the acoustic field, for an immersed boundary operating as a non-porous barrier, characterised by an impedance z_v, with parameters as indicated, and with admittance $y_p = 0$. The barrier cross section, of infinitesimal thickness, is indicated as a black line.

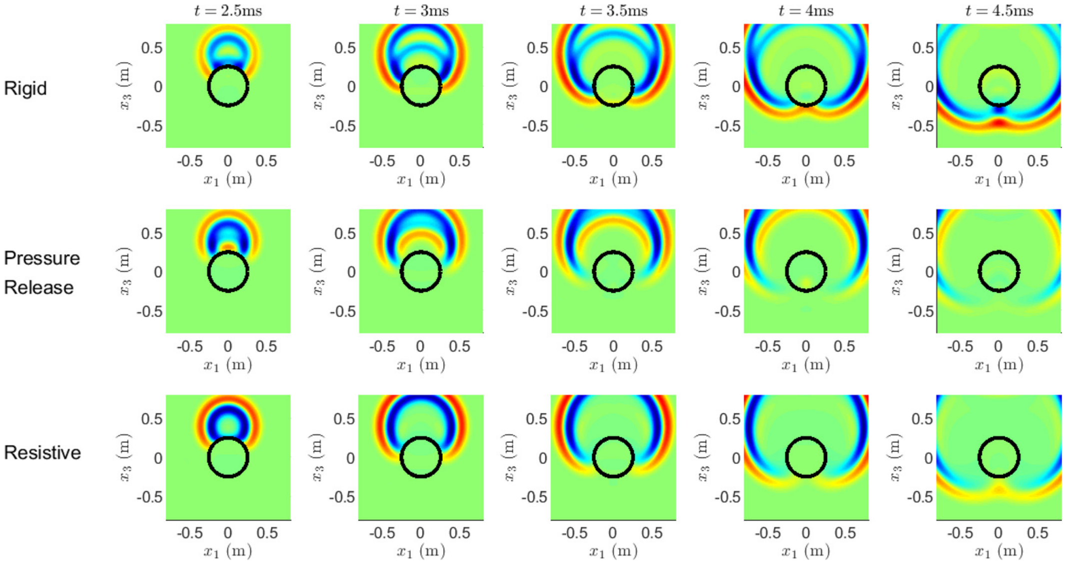

FIG. 7. (Color online) Time evolution of the acoustic field, for an immersed boundary operating as a non-porous barrier over a sphere, and for a point source, under different boundary conditions, as indicated.

release, and resistive cases, with $\alpha = 1$. Notice in particular the small amount of leakage visible within the sphere, particularly under rigid conditions. As before, a source signal with a high bandwidth has been chosen to illustrate this effect.

Exact solutions to the scattered acoustic field from a rigid sphere under a point source excitation are given by Hao *et al.*[39] and may be easily extended to the case of the more general condition (32) given above. Given a source excitation $u(t)$, applied at $\mathbf{x} = \mathbf{x}_s$, and a pressure signal $p_o(t)$ drawn from the acoustic field at $\mathbf{x} = \mathbf{x}_o$, with $R \leq |\mathbf{x}_o| \leq |\mathbf{x}_s|$, the solution, in free space, may be written as $p_o(t) = H(t) * u(t)$. The operator * indicates a convolution, and the kernel $H(t)$ may be recovered from the inverse Fourier transform of the following closed form expression for its transform $\hat{H}(\omega)$, where ω is the transform variable, an angular frequency in rad·s^{-1}:

$$\hat{H}(\omega) = \frac{i\omega\rho}{4\pi c}\sum_{l=0}^{\infty}(2l+1)P_l(\cos(\theta))h_l^{(2)}(\Theta_s) \times \left(-j_l(\Theta_o) + h_l^{(2)}(\Theta_o)\frac{j_l(\Theta)+i\alpha j_l'(\Theta)}{h_l^{(2)}(\Theta)+i\alpha h_l^{(2)\prime}(\Theta)}\right). \tag{33}$$

Here, $\Theta = \omega R/c$, $\Theta_s = \omega|\mathbf{x}_s|/c$, $\Theta_o = \omega|\mathbf{x}_o|/c$, and θ is the angle between $\mathbf{x}_s$ and $\mathbf{x}_o$, such that $\cos(\theta) = \mathbf{x}_s \cdot \mathbf{x}_o/|\mathbf{x}_s||\mathbf{x}_o|$. j_l and $h_l^{(2)}$ are the lth-order spherical Bessel function and spherical Hankel function of the second kind, respectively, j_l' and $h_l^{(2)\prime}$ are their derivatives, and P_l is the lth Legendre polynomial. The Fourier transform convention follows that of Ahrens.[40] A similar expression to the above is available in the case $R \leq |\mathbf{x}_s| \leq |\mathbf{x}_o|$. In practice, the infinite sum above must be truncated to a finite number of terms—here, 150, giving accuracy to one part in 10^{13} in all the simulation results below.

Comparisons between outputs taken from the computed field using the immersed boundary and exact solutions are shown in Fig. 8, for three outputs (labeled A, B, and C), drawn from a circle of radius 0.3 m in the (x_1, x_3) plane, on the near, lateral, and far sides of the sphere relative to the source location. Results are good in all cases, and in particular on the far side of the sphere, where the results are far superior to those obtained using standard FDTD boundary modeling methods, such as staircasing (detailed comparisons are presented in the case of a rigid sphere in recent work[27]).

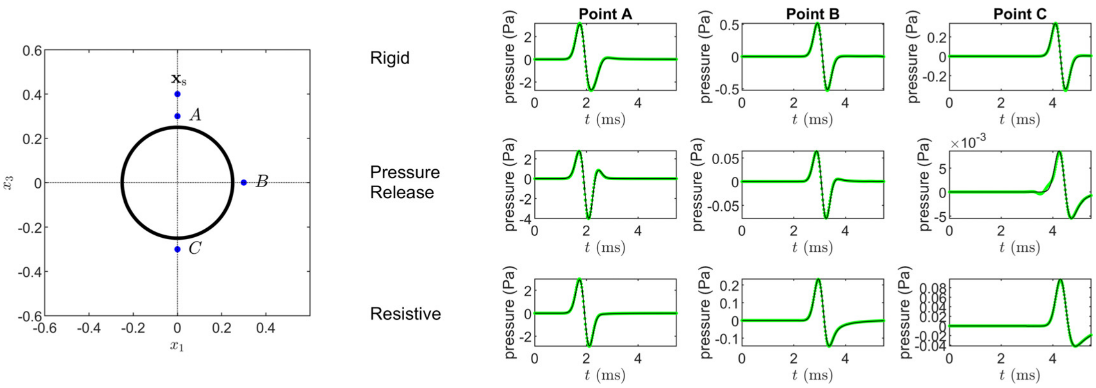

FIG. 8. (Color online) (Left) Cross section of a spherical immersed boundary, in the (x_1, x_3) plane, with source location $\mathbf{x}_s$ and output locations A, B, and C as indicated. (Right) Computed outputs (in green) and reference solutions (in black) at the three output locations, under rigid, pressure release, and resistive ($\alpha = 1$) conditions.

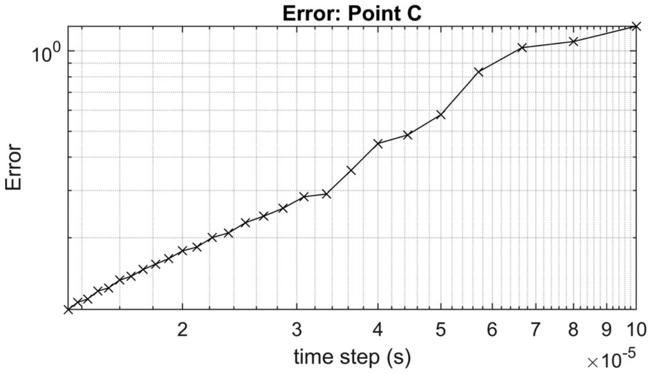

FIG. 9. Error, as defined in (34), for results of the simulation as described in the caption to Fig. 8, at point C, relative to the exact solution, at time steps as indicated.

To illustrate convergence behavior, under realistic conditions, consider output drawn from point C as illustrated in Fig. 8, on the far side of the sphere—the most stringent case. Conditions are assumed to be of rigid type. For a pressure waveform p^n_{out} drawn from point C, and given the exact solution p^n_{exact}, computed using (33), and over N_f samples, with time step T, define the normalized error as

$$\text{Error} = \sqrt{\frac{\sum_{n=0}^{N_f} T\left(p^n_{\text{out}} - p^n_{\text{exact}}\right)^2}{\sum_{n=0}^{N_f} T\left(p^n_{\text{exact}}\right)^2}}. \quad (34)$$

In Fig. 9, the error is plotted as function of time step, for steps corresponding to sampling rates ranging from 10 to 75 kHz in 5 kHz increments—first-order convergence is easily seen here. In addition to interpolation errors due to the approximation of the delta functions in the immersed boundary formulation, as well as numerical dispersion errors of the scheme, there are various factors that will influence the convergence rate, including (a) source and receiver interpolation errors and (b) slight variations in the Courant number due to the truncation of the number of grid points along each side dimension to an integer. These are not accounted for here.

V. CONCLUDING REMARKS

An immersed boundary method, specialised for use within room and architectural acoustics, has been demonstrated here. It is capable of simulating both impedance boundary conditions and barriers capable of acoustic transmission. The passive nature of scattering has been exploited to arrive at a framework for which there is no risk of numerical instability, beyond that of the numerical method operating in free space.

One of the main additional advantages of immersed boundary methods (besides the main advantage of the avoidance of volumetric meshing) is that they can be posed independently of the particular numerical method chosen. The methods in this article have been presented in a relatively agnostic form—basic FDTD methods are employed, but the results are more general and can extend to a much wider family of simulation techniques, including all those mentioned in Sec. I. All that is required is discrete representations of the Dirac delta function, of which only a few varieties have been discussed here. On the other hand, the stability analysis presented here (see the Appendix) is more restricted: The extension to other numerical methods will hinge on paired approximations to the gradient and divergence operations (and the maximal eigenvalue of the resulting negative discrete Laplacian) as well as the use of matched approximations to the Dirac delta function for both driving terms and field interpolation—a known requirement.[22]

The immersed boundary presented here has been used within a first-order system in pressure and velocity. More usual in wave-based and virtual acoustics is the numerical solution of the second-order wave equation in pressure alone—reducing the amount of storage required by a factor of approximately 2 in 3D. It would be of great interest to formulate the immersed boundary directly in terms of the second-order wave equation. Related to this is the question of the factorisablity of the discrete Laplacian into a gradient/divergence pair. The stability analysis in the Appendix relies on this, but for some of the most efficient and low-dispersion higher-order accurate wave equation solvers,[41,42] the discrete Laplacian is constructed directly and may not necessarily be factorisable. However, in the stability analysis, it is the maximal eigenvalue of the negative discrete Laplacian that determines the stability condition, so it may be expected that such analysis will extend to the case of the second-order wave equation.

One of the main computational costs is a $K \times K$ linear system solution at each time step, where K is the number of driving terms. For small scattering objects within a large space, this cost is very small in comparison with that required to update the field over the problem interior. There is a resemblance to the cost of boundary element method (BEM) calculation, but this is only superficial—in this case, the linear system to be solved is a constant, simple to compute and extremely sparse, in comparison with BEM, where the linear system is frequency-dependent, entries are in general difficult to compute, and the system is not sparse, unless fast multipole methods are employed.[43] The source of the linear system here is the use of the passivity-preserving integration rule used to model boundary/barrier immittances and to ensure numerical stability as a whole for the immersed boundary—see the Appendix. It would be possible to employ a different integration rule, in which case the linear system solution could be avoided, but at the cost of more extensive stability analysis. Here, however, the safest approach has been taken.

Not provided here is a full formal analysis of the errors incurred by the immersed boundary method—this is a very large undertaking, and well beyond the scope of this more applied article. Beyond the general numerical dispersion characteristics of the scheme, among the many factors that must be taken into consideration are (a) patch size relative to the underlying Cartesian grid spacing; (b) the use of flat patches to represent a curved surface, leading to some approximation error in terms of the total surface area of a given barrier; (c) the placement of a delta function within a given surface patch; and (d) the type of interpolant used.

ACKNOWLEDGMENTS

Thanks to Professor Jens Ahrens of Chalmers University of Technology for the verification of Eq. (33).

APPENDIX: NUMERICAL STABILITY

The analysis of numerical stability for the immersed boundary method as presented in Sec. III C is very similar to that of the 1D case[26] and is presented in brief here. As before, and as in previous work on related scenarios,[15,27] it relies on the determination of conditions under which all system poles have a non-positive real part.

Consider systems (28a) and (28b), alongside the K impedance relationships in (12c). Assume complex sinusoidal time dependence for all variables at frequency $s_d = \sigma_d + j\omega_d$, and, in particular, $\mathbf{p}^n = \hat{\mathbf{p}}e^{s_d nT}$, $\mathbf{v}^{n+1/2} = \hat{\mathbf{v}}e^{s_d T/2}e^{s_d nT}$ and $u^n = \hat{u}e^{s_d nT}$, for complex amplitudes $\hat{\mathbf{p}}$, $\hat{\mathbf{v}}$, and $\hat{u}$. After consolidation, the following system results:

$$\mathbf{H}\begin{bmatrix}\hat{\mathbf{p}}\\ \hat{\mathbf{v}}\end{bmatrix} = \begin{bmatrix}\dfrac{\lambda}{X^2}\mathbf{j}_s\hat{u}\\ 0\end{bmatrix}, \tag{A1}$$

where $\mathbf{H} = \mathbf{H}_0 + \mathbf{H}_{\text{IB}}$, with

$$\mathbf{H}_0 = \begin{bmatrix} 2\psi Y_0\mathbf{I}_{N_p} & \dfrac{\lambda}{\theta}\mathbf{D}^+\\ \dfrac{\lambda}{\theta}\mathbf{D}^- & 2\psi Z_0\mathbf{I}_{N_v}\end{bmatrix},$$
$$\mathbf{H}_{\text{IB}} = \begin{bmatrix}\mathbf{Q}_p\mathbf{Y}_p\mathbf{Q}_p^\top & \mathbf{0}\\ \mathbf{0} & \mathbf{Q}_v\mathbf{Z}_v\mathbf{Q}_v^\top\end{bmatrix}. \tag{A2}$$

Here, in $\mathbf{H}_0$, which encapsulates the behavior of scheme (28) in free space, $\psi = \tanh(s_d T/2)$, $\theta = \cosh(s_d T/2)$, and $\mathbf{I}_{N_p}$ and $\mathbf{I}_{N_v}$ are identity matrices of sizes $N_p \times N_p$ and $N_v \times N_v$, respectively. $\mathbf{H}_{\text{IB}}$, which encodes the behavior of the immersed boundary, depends on the constant matrices $\mathbf{Q}_p$ and $\mathbf{Q}_v$ defined by

$$\mathbf{Q}_p = \sqrt{2Y_0\lambda}\mathbf{J}_p\mathbf{S}^{1/2}, \quad \mathbf{Q}_v = \sqrt{2Z_0\lambda}\mathbf{N}_v\mathbf{S}^{1/2}. \tag{A3}$$

The diagonal $K \times K$ matrices $\mathbf{Y}_p$ and $\mathbf{Z}_p$ contain the immittances $y_p^{(k)}(\psi)$ and $z_v^{(k)}(\psi)$, $k = 1, \ldots, K$ on their diagonals, respectively. These immittances are obtained through the approximation $s \rightarrow \psi(s_d)$, corresponding to the trapezoid rule. Positive realness is preserved through this mapping so that, for any such discrete time immittance $w(\psi)$ obtained from a positive real immittance $w(s)$,

$$\text{Re}(w(\psi)) \geq 0 \quad \text{when} \quad \text{Re}(s_d) \geq 0, \tag{A4a}$$

$$\text{Im}(w(\psi)) = 0 \quad \text{when} \quad \text{Im}(s_d) = 0. \tag{A4b}$$

The natural frequencies of the system (A2) are determined by the zeros of $\mathbf{H}(s_d)$, or the frequencies $\bar{s}_d = \bar{\sigma}_d + j\bar{\omega}_d$ at which $\mathbf{H}$ drops rank. For numerical stability, it is necessary that $\bar{\sigma}_d \leq 0$. To examine this, suppose that $\mathbf{H}$ does drop rank at a frequency $\bar{s}_d$ with $\bar{\sigma}_d > 0$. It follows that there must exist complex-valued column vectors $\mathbf{f} \in \mathbb{C}^{N_p}$ and $\mathbf{g} \in \mathbb{C}^{N_v}$, not both zero, for which

$$W \triangleq [\mathbf{f}^* \quad \mathbf{g}^*]\,\mathbf{H}\begin{bmatrix}\mathbf{f}\\ \mathbf{g}\end{bmatrix} = \underbrace{[\mathbf{f}^* \quad \mathbf{g}^*]\,\mathbf{H}_0\begin{bmatrix}\mathbf{f}\\ \mathbf{g}\end{bmatrix}}_{W_0} + \underbrace{[\mathbf{f}^* \quad \mathbf{g}^*]\,\mathbf{H}_{\text{IB}}\begin{bmatrix}\mathbf{f}\\ \mathbf{g}\end{bmatrix}}_{W_{\text{IB}}}$$
$$= 0, \tag{A5}$$

where here, * indicates conjugate transposition. The two terms in (A5) above can be examined separately.

For W_0, the analysis is identical to that in the 1D case,[26] under the replacement of $\mathbf{D}_x^-$ with $\mathbf{D}^-$, and the following bound results:

$$\text{Re}(W_0) > 0 \quad \text{when} \quad \lambda < 2/e(\mathbf{D}^-), \tag{A6}$$

where $e(\mathbf{D}^-)$ is the largest singular value of the matrix $\mathbf{D}^-$. Considering W_{IB} in (A5), define the $K \times 1$ vectors $\tilde{\mathbf{f}} = \mathbf{Q}_p^\top\mathbf{f}$ and $\tilde{\mathbf{g}} = \mathbf{Q}_v^\top\mathbf{g}$. Thus,

$$W_{\text{IB}} = \tilde{\mathbf{f}}^*\mathbf{Y}_p\tilde{\mathbf{f}} + \tilde{\mathbf{g}}^*\mathbf{Z}_v\tilde{\mathbf{g}} = \sum_{k=1}^{K} y_p^{(k)}|\tilde{f}_k|^2 + z_v^{(k)}|\tilde{g}_k|^2. \tag{A7}$$

Because $y_p^{(k)}$ and $z_v^{(k)}$, $k = 1, \ldots, K$ are positive real, for $\text{Re}(\bar{s}_d) > 0$ it follows that

$$\text{Re}(W_{\text{IB}}) = \sum_{k=1}^{K} \text{Re}(y_p^{(k)})|\tilde{f}_k|^2 + \text{Re}(z_v^{(k)})|\tilde{g}_k|^2 \geq 0. \tag{A8}$$

Finally, from (A6) and (A8),

$$\text{Re}(W) > 0 \quad \text{when} \quad \lambda < 2/e(\mathbf{D}^-). \tag{A9}$$

As a result, (A5) does not hold for any $\bar{s}_d$ with $\bar{\sigma}_d > 0$, and, thus, scheme (28) has no system poles exhibiting exponential growth.

For $\mathbf{D}^\pm$ defined as in Sec. III, and under periodic or Neumann conditions, $e(\mathbf{D}^-) = \sqrt{12}$, and (A9) reduces to

$$\lambda < 1/\sqrt{3}. \tag{A10}$$

As in the 1D case,[26] this achieves the CFL condition (19) for the scheme defined in free space, with the case of equality ruled out.

[1] D. Botteldooren, "Acoustical finite-difference time-domain simulation in a quasi-Cartesian grid," J. Acoust. Soc. Am. **95**(5), 2313–2319 (1994).

[2] D. Botteldooren, "Finite-difference time-domain simulation of low-frequency room acoustic problems," J. Acoust. Soc. Am. **98**(6), 3302–3308 (1995).

[3] L. Savioja, T. Rinne, and T. Takala, "Simulation of room acoustics with a 3-D finite-difference mesh," in *Proceedings of the 1994 International Computer Music Conference*, Århus, Denmark (Michigan Publishing, Ann Arbor, MI, 1994), pp. 463–466.

[4] S. Bilbao, B. Hamilton, J. Botts, and L. Savioja, "Finite volume time domain room acoustics simulation under general impedance boundary conditions," IEEE/ACM Trans. Audio Speech Lang. Process. **24**(1), 161–173 (2016).

[5] M. Hornikx, W. De Roeck, and W. Desmet, "A multi-domain Fourier pseudospectral time-domain method for the linearized Euler equations," J. Comp. Phys. **231**(14), 4759–4774 (2012).

[6] F. Pind, A. Engsig-Karup, C. Jeong, J. Hesthaven, M. Mejling, and J. Strømann-Andersen, "Time domain room acoustic simulations using the spectral element method," J. Acoust. Soc. Am. **145**(6), 3299–3310 (2019).

[7] H. Wang, M. Cosnefroy, and M. Hornikx, "An arbitrary high-order discontinuous Galerkin method with local time-stepping for linear acoustic wave propagation," J. Acoust. Soc. Am. **149**(1), 569–580 (2021).

[8] R. Dragonetti and R. Romano, "Errors when assuming locally reacting boundary condition in the estimation of the surface acoustic impedance," Appl. Acoust. **115**, 121–130 (2017).

[9] E. Williams, *Fourier Acoustics; Sound Radiation and Nearfield Acoustical Holography* (Academic, London, 1999).

[10] H. Wang, J. Yang, and M. Hornikx, "Frequency-dependent transmission boundary condition in the acoustic time-domain nodal discontinuous Galerkin model," Appl. Acoust. **164**, 107280 (2020).

[11] S. Prepeliă, M. Geronazzo, F. Avanzini, and L. Savioja, "Influence of voxelization on finite difference time domain simulations of head-related transfer functions," J. Acoust. Soc. Am. **139**(5), 2489–2504 (2016).

[12] M. Toyoda and S. Ishikawa, "Frequency-dependent absorption and transmission boundary for the finite-difference time-domain method," Appl. Acoust. **145**, 159–166 (2019).

[13] M. Berger and R. LeVeque, "Stable boundary conditions for Cartesian grid calculations," Comp. Syst. Eng. **1**(2–4), 305–311 (1990).

[14] M. Berger and A. Giuliani, "A state redistribution algorithm for finite volume schemes on cut cell meshes," J. Comput. Phys. **428**, 1–20 (2021).

[15] S. Bilbao and B. Hamilton, "Passive volumetric time domain simulation for room acoustics applications," J. Acoust. Soc. Am. **145**(4), 2613–2624 (2019).

[16] C. Peskin, "Flow patterns around heart valves: A numerical method," J. Comput. Phys. **10**, 252–271 (1972).

[17] C. Peskin, "The immersed boundary method," Acta Numer. **11**, 479–517 (2002).

[18] W. Huang and F. Tian, "Recent trends and progress in the immersed boundary methods," J. Mech. Eng. Sci. **233**, 7617–7636 (2019).

[19] A. Bhalla, R. Bale, B. Griffith, and N. Patankar, "A unified mathematical framework and an adaptive numerical method for fluid-structure interaction with rigid, deforming and elastic bodies," J. Comput. Phys. **250**, 446–476 (2013).

[20] D. Goldstein, R. Handler, and L. Sirovich, "Modeling a no-slip flow boundary with an external force field," J. Comput. Phys. **105**, 354–366 (1993).

[21] X. Sun, Y. Jiang, A. Liang, and X. Jing, "An immersed boundary computational model for acoustic scattering problems with complex geometries," J. Acoust. Soc. Am. **132**(5), 3190–3199 (2012).

[22] B. Kallemov, A. Bhalla, B. Griffith, and A. Donev, "An immersed boundary method for rigid bodies," Commun. Appl. Math. Comp. Sci. **11**(1), 79–141 (2016).

[23] R. Mittal and G. Iaccarino, "Immersed boundary methods," Annu. Rev. Fluid Mech. **37**, 239–261 (2005).

[24] J. Seo and R. Mittal, "A high-order immersed boundary method for acoustic wave scattering and low-Mach number flow-induced sound in complex geometries," J. Comput. Phys. **230**(4), 1000–1019 (2011).

[25] S. Péron, C. Benoit, T. Renaud, and I. Mary, "An immersed boundary method on Cartesian adaptive grids for the simulation of compressible flows around arbitrary geometries," Eng. Comput. **37**, 2419–2437 (2021).

[26] S. Bilbao, "Modeling impedance boundary conditions and acoustic barriers using the immersed boundary method: The one-dimensional case," J. Acoust. Soc. Am. **153**(4), 2023–2036 (2023).

[27] S. Bilbao, "Immersed boundary methods in wave-based virtual acoustics," J. Acoust. Soc. Am. **151**(3), 1627–1638 (2022).

[28] S. Bilbao, "Impedance boundaries and transmission in wave-based acoustics using the immersed boundary method," in *Proceedings of the International Congress on Acoustics*, Gyeongju, South Korea (2022).

[29] O. Brune, "Synthesis of a finite two-terminal network whose driving-point impedance is a prescribed function of frequency," Ph.D. thesis, Massachusetts Institute of Technology, Cambridge, MA, 1931.

[30] X. Yang, X. Zhang, Z. Li, and G. He, "A smoothing technique for discrete delta functions with application to immersed boundary method in moving boundary simulations," J. Comput. Phys. **228**(6), 7821–7836 (2009).

[31] S. Bilbao, "3D acoustic field interpolation in wave-based simulation," IEEE Signal Process. Lett. **29**, 384–388 (2022).

[32] M. Woodbury, *Inverting Modified Matrices* (Princeton University, Princeton, NJ, 1950).

[33] Y. Saad, *Iterative Methods for Sparse Linear Systems*, 2nd ed. (SIAM, Philadelphia, 2003).

[34] B. Engquist and A. Majda, "Absorbing boundary conditions for the numerical simulation of waves," Math. Comput. **31**(139), 629–651 (1977).

[35] J. Strikwerda, *Finite Difference Schemes and Partial Differential Equations* (Wadsworth and Brooks/Cole Advanced Books and Software, Pacific Grove, CA, 1989).

[36] R. Duda and W. Martens, "Range dependence of a spherical head model," J. Acoust. Soc. Am. **104**(5), 3048–3058 (1998).

[37] B. Katz, "Boundary element method calculation of individual head-related transfer function. II. Impedance effects and comparisons to real measurements," J. Acoust. Soc. Am. **110**(5), 2449–2455 (2001).

[38] C. Koay, "Analytically exact spiral scheme for generating uniformly distributed points on the unit sphere," J. Comp. Sci. **2**(1), 88–91 (2011).

[39] J. Hao, R. Kotapati, F. Pérot, and A. Mann, "Numerical studies of acoustic diffraction by rigid bodies," in *Proceedings of the 22nd AIAA/CEAS Aeroacoustics Conference*, Lyon, France American Institute of Aeronautics and Astronautics, Reston, VA (2016).

[40] J. Ahrens, *Analytic Methods of Sound Field Synthesis* (Springer, Heidelberg, Germany, 2012), p. 30.

[41] J. Tuomela, "On the construction of arbitrary order schemes for the many-dimensional wave equation," BIT Numer. Math. **36**(1), 158–165 (1996).

[42] S. Bilbao and B. Hamilton, "Higher-order accurate two-step finite difference schemes for the many-dimensional wave equation," J. Comput. Phys. **367**, 134–165 (2018).

[43] N. Gumerov and R. Duraiswami, "Fast multipole accelerated boundary element methods for room acoustics," J. Acoust. Soc. Am. **150**(3), 1707–1720 (2021).